Nano Research

Open Access

Research Article

Hierarchical NiFe LDH/N-doped Co/nickel foam as highly active oxygen evolution reaction electrode for anion exchange membrane water electrolysis

Jiansheng Wang[1,2], Yongsheng Wang[1,2], Xiaoxuan Guo[1,2], Mengting Chen[1,2], Jinjie Fang[3], Xiaojie Li[3], Wei Zhu[1,2] ✉, and Zhongbin Zhuang[1,2] ✉

[1] *State Key Lab of Organic-Inorganic Composites and Beijing Advanced Innovation Center for Soft Matter Science and Engineering, Beijing University of Chemical Technology, Beijing 100029, China*
[2] *Beijing Key Laboratory of Energy Environmental Catalysis, Beijing University of Chemical Technology, Beijing 100029, China*
[3] *PetroChina Shenzhen New Energy Research Institute Co., Ltd., Shenzhen 518054, China*

Cite this article: *Nano Research*, **2025**, *18*, 94907190. https://doi.org/10.26599/NR.2025.94907190

ABSTRACT: Anion exchange membrane water electrolyzers (AEMWEs) are emerging as a promising technology due to the high performance and low cost. However, the development of highly active and stable non-precious metal-based catalysts for the anodic oxygen evolution reaction (OER) remains a great challenge. In this study, we present a top-down construction strategy for anode design, resulting in a hierarchical NiFe layered double hydroxide (LDH)/N-doped Co/nickel foam (NF) electrode synthesized via a hydrothermal-gas phase nitridation–electrodeposition method. This electrode features NiFe LDH nanoplates grown on N-doped Co nanowires supported by nickel foam substrates. The NiFe LDH/N-doped Co/NF electrode demonstrates exceptional performance, achieving a current density of 100 mA·cm^{-2} at a low overpotential of 262 mV with minimal attenuation of just 7 mV after 100 h of operation. When assembled into an AEMWE, the system requires only 1.63 V to achieve a current density of 1 A·cm^{-2}, surpassing the performance of most reported catalysts. The N-doped Co nanowires are shown to enhance both activity and stability by increasing the electrode's surface area and reinforcing the catalyst–support interaction.

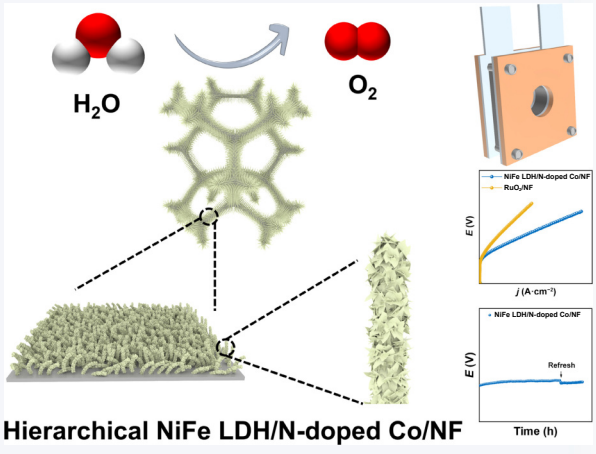

Hierarchical NiFe LDH/N-doped Co/NF

KEYWORDS: water electrolysis, oxygen evolution reaction, hierarchical structure, synergistic effect

1 Introduction

Hydrogen is widely regarded as an ideal energy carrier for sustainable energy systems due to its high energy density and the non-polluting nature of its combustion products [1–3]. Currently, hydrogen production is predominantly achieved through steam reforming, underscoring the urgent need for sustainable and green hydrogen production technologies to meet growing demand [4–11]. Among these, water electrolysis has emerged as an efficient approach for renewable energy storage, enabling the conversion of electrical energy into hydrogen energy [12, 13]. Notably, anion exchange membrane water electrolysis (AEMWE) distinguishes itself through high efficiency and the ability to employ non-precious metal electrodes, offering a cost-effective solution for industrial-scale applications.[14]

Despite these advantages, the oxygen evolution reaction (OER) at the anode of AEMWEs encounters significant kinetic barriers due to its sluggish four-electron transfer mechanism. These challenges are further exacerbated by the dissolution and exfoliation of non-precious metal catalysts under highly oxidative conditions [15–19]. Enhancing the energy efficiency and durability of AEMWEs is therefore critical for reducing hydrogen production costs and enabling scalable commercialization [20]. Research efforts have focused on the rational design and synthesis of non-precious metal catalysts with high activity and stability for OER in alkaline

Received: November 26, 2024; **Revised:** December 13, 2024
Accepted: December 13, 2024

✉Address correspondence to Wei Zhu, zhuwei@mail.buct.edu.cn; Zhongbin Zhuang, zhuangzb@mail.buct.edu.cn

conditions [21, 22]. Transition metal-based materials, such as alloys [23], sulfides [24], phosphides [25], nitrides [26], and hydroxides [27], have been extensively investigated. Among these, NiFe layered double hydroxides (LDHs) exhibit exceptional OER activity [28, 29], attributed to the accelerated formation of MOOH intermediates and interlayer anions that enhance reaction kinetics by modulating the lattice structure [30].

Recent studies highlight promising advancements. For instance, Zheng et al. synthesized lattice-contracted NiFe LDH, achieving a low overpotential of 217 mV at 10 mA·cm^{-2} with good durability over 20 h [31]. Xing et al. developed a zipper-like interlocked heterostructure of NiFe LDH-WN that demonstrated ultrahigh OER activity, achieving 228 mV of overpotential at 50 mA·cm^{-2} and excellent long-term stability [32]. However, in AEMWE devices, powdered catalysts are typically bound to porous transport layers (PTLs) using electrically insulating binders (e.g., anion exchange membrane (AEM) ionomers, Nafion, and polytetrafluroethylene (PTFE)), which compromise electrical conductivity and mass transport, particularly at high industrial current densities [33–36].

To address these limitations, researchers have explored self-supported electrodes by growing NiFe LDH catalyst layers (CLs) directly on PTLs. This binder-free approach reduces the overall internal resistance of the anode catalytic layer [37]. Nevertheless, the low intrinsic conductivity of high-loading NiFe LDH remains a bottleneck for OER performance [38]. Introducing an intermediate conductive layer with strong interfacial interactions between the NiFe LDH and PTL has shown promise for enhancing device performance at industrial current densities [39]. Additionally, nanowire (NW) array structures endow electrodes with superhydrophilic properties, enabling efficient gas–liquid mass transfer and reducing mass transport resistance [40].

In this study, we present a hierarchical electrode design comprising a three-dimensional porous nickel foam (NF) as the PTL, a two-dimensional NiFe LDH as the OER CL, and a one-dimensional nitrogen-doped cobalt (N-doped Co) NW interlayer. This architecture aims to enhance catalytic activity and stability. The self-supported NiFe LDH/N-doped Co/NF electrode was fabricated using a hydrothermal-gas phase nitridation–electrodeposition synthesis method. The electrode exhibited outstanding performance, achieving a current density of 100 mA·cm^{-2} at a low overpotential of 262 mV in 1 M KOH and maintaining excellent stability over 100 h of operation. When assembled into an AEMWE device, the electrode achieved a current density of 4.84 A·cm^{-2} at a cell voltage of 2.0 V with minimal performance decay during a 90-h stability test at 1 A·cm^{-2}. Control experiments and characterization analyses revealed that the N-doped Co NWs imparted high surface area and superhydrophilic properties to the electrode and effectively reduced both internal and charge transfer resistances, significantly enhancing OER performance.

2 Experimental

2.1 Materials

NFs with a thickness of 1.5 mm, a packing density of 320 g·m^{-2}, and a purity of 99.8% were purchased from Kunshan Guangjiaoyuan New Material Co. HCl (36 wt.%) and anhydrous ethanol (99.8%) were purchased from Beijing Tongguang Fine Chemical Company. $Ni(NO_3)_2·6H_2O$ (analytical reagent (AR)), $Co(NO_3)_2·6H_2O$ (AR), $FeSO_4·7H_2O$ (AR), NH_4F (AR), $CO(NH_2)_2$ (AR), and NH_4Cl (AR) were purchased from Shanghai Aladdin Biochemical Technology. Commercial PtRu/C and RuO_2 were purchased from SCI Materials Hub. All chemicals were used as received without further purification and all water used for synthesis and analysis was purified to > 18.2 MΩ·cm by Millipore system.

2.2 Preparation of $Co(OH)_x$/NF

Prior to the preparation of $Co(OH)_x$/NF, NF with a surface density of 320 g·m^{-2} and a thickness of 1.5 mm was pressed to a thickness of 270 μm using a roller press. 2 cm × 3 cm of NF was then sonicated with acetone and 3 M HCl for 30 min each, followed by washing with deionized water and anhydrous ethanol to remove surface grease and oxides.

$Co(OH)_x$/NF was prepared using a hydrothermal method. 1 mmol of $Co(NO_3)_2·6H_2O$, 2 mmol of NH_4F, and 5 mmol of $CO(NH_2)_2$ were dissolved in 40 mL of deionized water and stirred for 20 min. The solution and the processed NF were then transferred to a 50 mL autoclave and kept at 120 °C for 6 h. After cooling to room temperature, the sample was rinsed with deionized water and dried overnight.

2.3 Preparation of N-doped Co/NF

The N-doped Co NWs on NF were prepared by the nitridation of the as-obtained $Co(OH)_x$/NF. A porcelain boat with 500 mg of $CO(NH_2)_2$ was positioned upstream of a quartz tube, while a porcelain boat with $Co(OH)_x$/NF was placed downstream. The nitridation was conducted at 450 °C with a ramp rate of 5 °C per minute for 120 min under a nitrogen atmosphere.

2.4 Preparation of NiFe LDH/N-doped Co/NF

The NiFe LDH/N-doped Co/NF electrode was prepared by the on-site growth of NiFe-LDH nanosheets on the N-doped Co/NF using an electrodeposition method. A solution was prepared by dissolving 0.01 mol (2.91 g) of $Ni(NO_3)_2·6H_2O$, 0.01 mol (2.78 g) of $FeSO_4·7H_2O$, and 0.1 mol (5.3 g) of NH_4Cl in 100 mL of deionized water. The electrodeposition was carried out in a two-electrode system, with N-doped Co/NF as the working electrode and graphite flakes as the counter electrode. The deposition was conducted at a current density of 75 mA·cm^{-2} for 60 s. After electrodeposition, the sample was rinsed with deionized water and dried overnight.

2.5 Preparation of other comparison samples

The synthetic procedure of NiFe LDH/$Co(OH)_x$/NF was the same as for the NiFe LDH/N-doped Co/NF electrodeposition, except that the N-doped Co/NF precursor was replaced with $Co(OH)_x$/NF. The synthetic procedure of NiFe LDH/NF was the same as for the NiFe LDH/N-doped Co/NF electrodeposition, except that the N-doped Co/NF precursor was replaced with NF.

2.6 Preparation of RuO_2/NF

5.0 mg of RuO_2 was dissolved in a mixture of 240 μL of deionized water, 750 μL of isopropanol, and 10 μL of 5% Nafion. The mixture was first subjected to 3 min of vigorous sonication in an ice bath, followed by 2 h of sonication to form a well-dispersed catalyst ink. This ink was then drop-coated onto a 1 cm^2 NF substrate with a loading of 1 mg·cm^{-2}.

2.7 Electrochemical measurements

Electrochemical measurements were performed using a CHI-760

electrochemical workstation (CHI Instrument) in a three-electrode system. The tests were maintained at a constant temperature of 30 °C in a 1 M KOH solution with oxygen saturation. The synthesized catalyst was used as the working electrode, while Hg/HgO and carbon rod served as the reference and counter electrodes, respectively. All potentials were converted to reversible hydrogen electrode (RHE) potentials using Eq. (1)

$$E_{(\text{vs. RHE})} = E_{(\text{vs. Hg/HgO})} + 0.098 + 0.0591 \times \text{pH} \quad (1)$$

Polarization curves were obtained via linear scanning voltammetry (LSV) with a scanning rate of 5 mV·s^{-1} and 100% *iR* compensation at a potential of 0.6 V (vs. HgO/Hg). Electrochemical impedance spectroscopy (EIS) were recorded in the frequency range of 100 kHz to 0.1 Hz, and the OER stability was assessed by chronopotentiometry for 100 h at a current density of 100 mA·cm^{-2}. The electrochemical surface area (ECSA) was determined by measuring the double-layer capacitance (C_{dl}) in the non-Faradaic region, under an Ar atmosphere, at various cyclic voltammetry (CV) scanning rates. ECSA was calculated using Eq. (2)

$$\text{ECSA} = C_{dl}/C_s \quad (2)$$

where C_s is typically assumed to be 0.04 mF·cm^{-2} for Ni/Co-based materials.

2.8 AEMWE fabrications and tests

The membrane electrode assembly (MEA) was prepared using the catalyst-coated substrate (CCS) technique. The cathode was made by spraying a PtRu/C catalyst ink onto carbon paper (HCP030N) with a loading of 0.3 mg_{Pt}·cm^{-2}. The anode was prepared using the synthesized NiFe LDH/N-doped Co/NF and RuO_2/NF control samples. The electrodes had an effective area of 4 cm^2 and a loading capacity of 1.25 mg·cm^{-2}. The anion exchange membrane was PiperION™ A20 (20 μm), which was soaked in 1 M KOH solution overnight. The anion exchange membrane, CCS, stainless steel runner plate with a 4 cm^2 flow field, and metal bipolar plate were assembled to form a complete AEMWE. The performance of the AEMWE was evaluated at 60 °C and 1 M KOH.

2.9 Characterization

The catalysts were analyzed for their chemical composition and microstructure using various analytical methods. The microstructure was examined with transmission electron microscopy (TEM, FEI Talos F200x) and scanning electron microscopy (SEM, TESCAN Clara). The crystalline phase was analyzed using X-ray diffraction (XRD, Rigaku D/Max 2500 VB2+/PC) with a sweep rate of 5 °·min^{-1} and a scanning angle range of 2θ from 10° to 90°. X-ray photoelectron spectroscopy (XPS, Thermo Scientific K-Alpha) with an Al Kα excitation source ($h\nu$ = 1486.8 eV) was employed to analyze the chemical states of the catalyst. Raman spectroscopy (Renishaw inVia Reflex) was used to determine the chemical and molecular structures of the samples. Inductively coupled plasma mass spectrometry (ICP-MS, Agilent 7800) was employed to analyze the concentrations of metallic elements in the solution. A high-speed camera (X-Motion, AOS technologies) was used for droplet contact angle photography.

3 Results and discussion

3.1 Characterization of the hierarchical NiFe LDH/N-doped Co/NF

A facile three-step process was employed to synthesize the hierarchical NiFe LDH/N-doped Co/NF, as shown in Fig. 1(a).

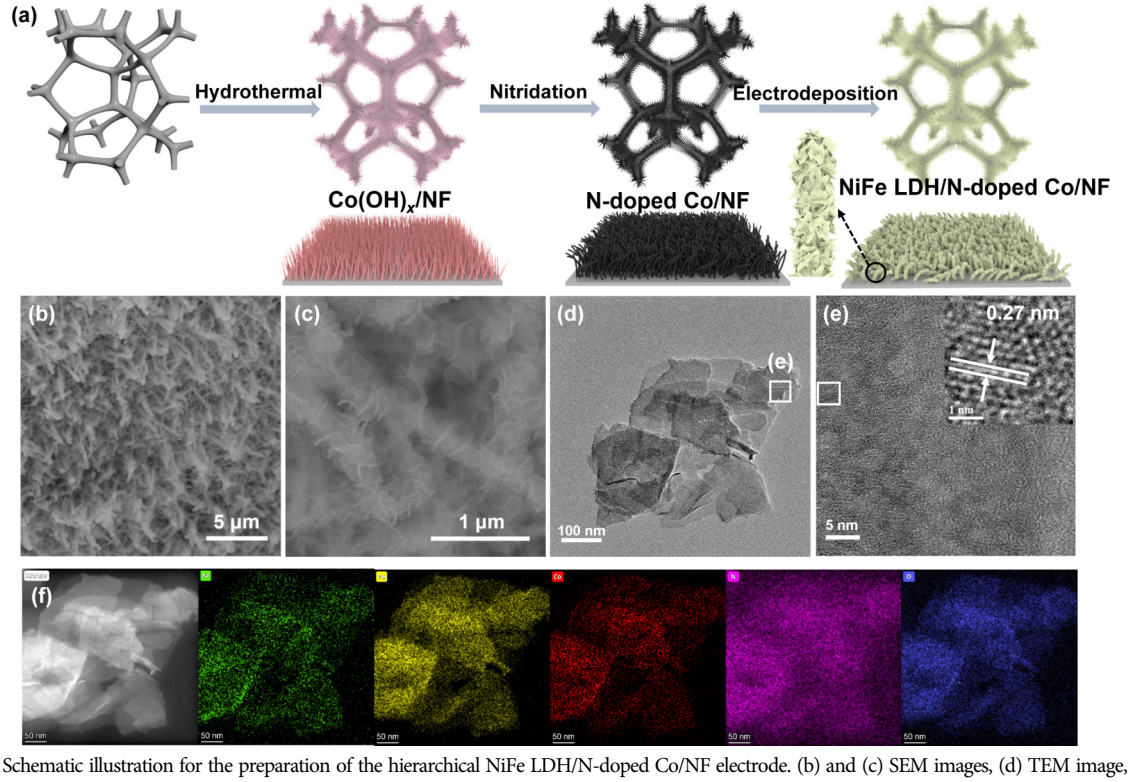

Figure 1 (a) Schematic illustration for the preparation of the hierarchical NiFe LDH/N-doped Co/NF electrode. (b) and (c) SEM images, (d) TEM image, (e) HRTEM image, and (f) HAADF-STEM elemental mapping images of the NiFe LDH/N-doped Co/NF electrode.

First, $Co(OH)_x$ NW arrays were grown on NF using a hydrothermal method. Next, the $Co(OH)_x$ precursor was reduced and nitrided through a gas-phase thermal treatment using urea as the nitrogen source and converted into N-doped Co NWs. In the process, urea upstream underwent the pyrolysis process to produce NH_3 at 450 °C. The reductive NH_3 reduced the $Co(OH)_x$ to Co. NH_3 also served as the N source in the synthesis, and it reacted with a portion of Co to form N-doped Co. The NW structure was retained in the nitridation. Finally, the NiFe LDH nanosheets were grown on the N-doped Co/NF via an electrodeposition method, forming the hierarchical NiFe LDH/ N-doped Co/NF. Figures S1(a) and S1(b) in the Electronic Supplementary Material (ESM) show the corresponding SEM images, displaying that $Co(OH)_x$ NWs grew on the NF surface uniformly. After nitridation treatment, the NWs morphology was retained (Figs. S1(c) and S1(d) in the ESM) with the increase in surface roughness. At last, NiFe LDH was deposited onto the N-doped Co NWs by electrodeposition. As shown in Figs. 1(b) and 1(c), NiFe LDH nanosheets were uniformly deposited onto the NWs array. Additionally, in the absence of nitridation treatment, similar NiFe LDH nanosheets with a larger size were formed on the $Co(OH)_x$ NWs (Fig. S2 in the ESM). When the NiFe LDH was directly electrodeposited onto the relatively smooth NF substrate, the size became even larger (Fig. S3 in the ESM). It was deduced that the improved electrical conductivity of N-doped Co provided more sites for the metal ions deposition during the electrodeposition and thus resulted in small-sized and uniform NiFe LDH nanosheets. Hence, the increased surface roughness and the improved conductivity by the N-doped Co NW contributed to the formation of small-sized and uniform NiFe LDH CLs.

The N-doped Co NWs and the corresponding $Co(OH)_x$ precursor were exfoliated from the NF substrates using the N-doped Co/NF and $Co(OH)_x$/NF samples, respectively, and were subsequently characterized by XRD and TEM (Figs. S4 and S5 in the ESM). The XRD results suggested the interlayer converted from cobalt carbonate hydroxide to metallic status during the gas-phase nitridation treatment. Reductive NH_3 generated from urea triggered the reduction of the Co-based precursor. Figure S5 in the ESM shows the TEM image of the N-doped Co NWs, and the NWs with a width of 50 nm. The crystal structure of N-doped Co NWs was revealed by high-resolution TEM (HRTEM) images (Fig. S5(b) in the ESM), showing that the lattice fringe spacings of 0.177 and 0.205 nm were correlated to the (200) and (111) crystal planes of cubic Co, respectively. The selected area electron diffraction (SAED) pattern in Fig. S5(c) in the ESM also confirmed that the NW crystal structure was assigned to Co, consistent with the XRD results. Additionally, the elemental mapping profiles (Figs. S5(d) and S5(e) in the ESM) suggested the doping of nitrogen with an atomic Co:N ratio of 95.4:4.6, thereby validating the formation of N-doped Co.

The XRD spectra of NiFe LDH/N-doped Co/NF, NiFe LDH/$Co(OH)_x$/NF, NiFe LDH/NF, and their precursors N-doped Co/NF and $Co(OH)_x$/NF are shown in Figs. S6 and S7 in the ESM. The XRD patterns only showed intensive diffraction peaks of NF without the detectable signals from the NiFe LDH catalysts due to the low loading of the electrocatalysts on the NF. As shown in Fig S7 in the ESM, the spacing observed in HRTEM image suggests that the absence of signals from NiFe LDH-related physical phase peaks in XRD is due to low surface loading. As shown in Figs. 1(d) and 1(e), the lattice fringe spacing of 0.27 nm was assigned to the (101) crystal plane of NiFe LDH (JCPDS #40-0215) [41]. Figure S8 in the ESM shows the morphological characteristics of the NiFe LDH surface. The fast Fourier transform pattern and the short-range ordered lattice fringes suggested the polycrystalline surface structure. The spacing also matched the NiFe LDH characteristics. Abundant defective nanomesh structures in low contrast distributed across the surface of NiFe LDH at a scale of 3–4 nm uniformly. This was attributed to the short electrodeposition process, which created a substantial number of coordinatively unsaturated sites during the growth of NiFe LDH. The bright field/high-angle annular dark-field scanning TEM (HAADF-STEM) elemental mapping (energy dispersive X-ray spectroscopy (EDS)) profiles (Fig. 1(f)) show the uniform distribution of Ni, Fe, Co, N, and O elements.

To further investigate the chemical valence, XPS was also performed on the NiFe LDH/N-doped Co/NF and the other two references (i.e., NiFe LDH/NF and N-doped Co/NF). Figure S9 in the ESM shows the XPS survey spectra. The presence of Ni, Fe, Co, and O elements was consistent with the EDS result. However, the composition of N from XPS was lower than that from EDS, which was probably because XPS is surface-sensitive and the surface of N-doped Co NWs was covered by the NiFe LDH. The Ni 2p high-resolution XPS spectra are shown in Fig. 2(a). Two distinct peaks at 855.76 and 873.37 eV in NiFe LDH/N-doped Co/NF were attributed to the Ni^{2+} $2p_{3/2}$ and $2p_{1/2}$ peaks, respectively, while the two peaks located at 861.50 and 879.22 eV were the satellite peaks. The NiFe LDH/N-doped Co/NF showed a negative shift of 0.2 eV as compared to the NiFe LDH/NF. The high-resolution XPS spectra of Fe 2p are shown in Fig. 2(b). The peaks at 710.98 and 724.18 eV were corresponding to Fe^{2+} $2p_{3/2}$ and $2p_{1/2}$, while the peaks at 713.78 and 729.98 eV were assigned to Fe^{3+} $2p_{3/2}$ and $2p_{1/2}$, respectively. The negative shift of the binding energies of Ni 2p and Fe 2p in NiFe LDH/N-doped Co/NF compared to NiFe LDH/NF implied that the N-doped Co NWs played the role of electron donor in the composite electrodes. The high-resolution XPS spectra of Co 2p are shown in Fig. 2(c). The peaks at 780.98 and 796.78 eV corresponded to the Co^{2+} $2p_{3/2}$ and $2p_{1/2}$, respectively. The N-doped Co NWs exhibited a Co^0 peak at 777.48 eV, but it disappeared after the loading of the NiFe LDH CL. It might be attributed to the charge transfer between the NiFe LDH and the N-doped Co NWs, leading to the oxidation of metallic Co. Additionally, a positive shift of 0.6 eV was observed when compared to N-doped Co/NF, suggesting the probable charge transfer from Co to NiFe LHD. The high-resolution XPS spectra of O 1s for NiFe LDH/N-doped Co/NF are shown in Fig. 2(d). The peaks at 529.58, 531.18, and 532.88 eV corresponded to metal–O bonds (M–O), metal–OH (M–OH), and adsorbed oxygen species (O_{ads}), respectively. The O 1s binding energy of the NiFe LDH/N-doped Co/NF shifted to a lower position compared to that of NiFe LDH/NF. It was also suggested the probable charge transfer from the N-doped Co NWs to the NiFe LDH. The high-resolution XPS spectrum of N 1s is shown in Fig. S10 in the ESM. The main peak located at 397.68 eV corresponded to the metal–N bond, verifying the doping of N into Co, while the small peak located at 399.68 eV was attributed to the N–H bond.

3.2 Electrochemical performance of NiFe LDH/N-doped Co/NF

The OER electrochemical performance of the NiFe LDH/N-doped Co/NF electrode was evaluated in the 1 M KOH electrolyte. As shown in Fig. 3(a), a distinct oxidation peak was observed for NiFe

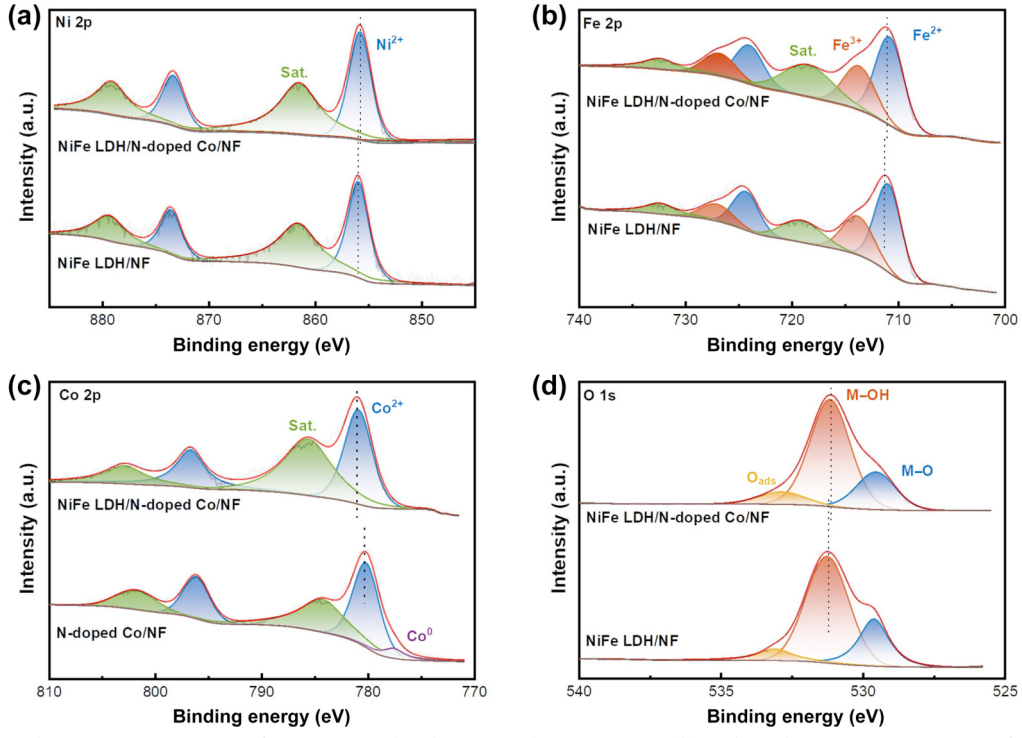

Figure 2 (a) High-resolution Ni 2p XPS spectra of NiFe LDH/N-doped Co/NF and NiFe LDH/NF. (b) High-resolution Fe 2p XPS spectra of NiFe LDH/N-doped Co/NF and NiFe LDH/NF. (c) High-resolution Co 2p XPS spectra of NiFe LDH/N-doped Co/NF and N-doped Co/NF. (d) High-resolution O 1s XPS spectra of NiFe LDH/N-doped Co/NF and NiFe LDH/NF.

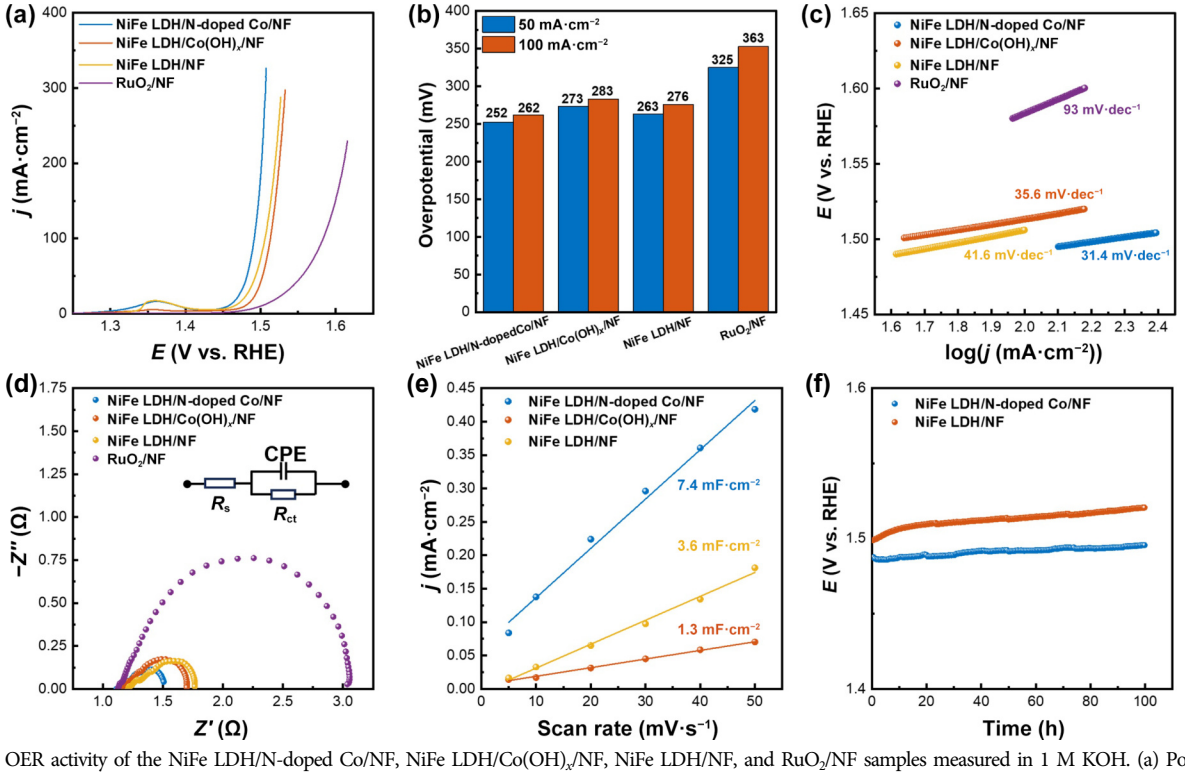

Figure 3 OER activity of the NiFe LDH/N-doped Co/NF, NiFe LDH/Co(OH)$_x$/NF, NiFe LDH/NF, and RuO_2/NF samples measured in 1 M KOH. (a) Polarization curves for OER process. (b) Overpotential histograms at 50 and 100 mA·cm^{-2}. (c) Tafel slopes of the electrocatalysts. (d) Nyquist plots of the electrocatalysts. (e) C_{dl}. (f) Chronopotentiometric curves at 100 mA·cm^{-2}.

LDH/N-doped Co/NF near the potential of 1.35 V (vs. RHE), which was attributed to the oxidation of Ni^{2+} to Ni^{3+}. Figure 3(b) shows the overpotentials at different current densities for the catalysts. The overpotentials of these samples at 50 and 100 mA·cm^{-2} of current densities were denoted as η_{50} and η_{100}, respectively. The NiFe LDH/N-doped Co/NF showed the lowest η_{50} and η_{100} values amongst the tested catalysts, requiring only 252 and 262 mV to achieve the current densities of 50 and 100 mA·cm^{-2},

respectively. The low overpotential of NiFe LDH/N-doped Co/NF demonstrated high activity, which was comparable to most of the NiFe-based electrocatalysts for OER (Table S1 in the ESM) [41–50]. The NiFe LDH/Co(OH)$_x$/NF (η_{50} = 273 mV and η_{100} = 283 mV) and NiFe LDH/NF (η_{50} = 263 mV and η_{100} = 276 mV) exhibited the inferior OER activity than the NiFe LDH/N-doped Co/NF but surpassed the commercial RuO_2 on the NF (η_{50} = 325 mV and η_{100} = 363 mV) significantly. The OER activity of the NiFe LDH/Co(OH)$_x$/NF was slightly lower than that of the NiFe LDH/NF, while the OER activity of the NiFe LDH/N-doped Co/NF was much higher than that of the NiFe LDH/NF. It suggested the significance of the nitridation step by improving the electrical conductivity from Co(OH)$_x$ to N-doped Co. Hence, the electrical-conductive N-doped Co interlayer enabled the high utilization of the surface NiFe LDH sites and contributed to the superior OER activity. As shown in Fig. S11 in the ESM, the OER performance of N-doped Co/NF was also evaluated. The overpotential of N-doped Co/NF was much larger than that of NiFe LDH/N-doped Co/NF, suggesting that the superior OER activity resulted from the synergistic effect between the NiFe LDH catalyst and the N-doped Co NW interlayer. Figure 3(c) shows the corresponding Tafel plots. The Tafel slope of NiFe LDH/N-doped Co/NF was 31.4 mV·dec^{-1}, which was comparable to those of NiFe LDH/Co(OH)$_x$/NF (35.6 mV·dec^{-1}) and NiFe LDH/NF (41.6 mV·dec^{-1}). The Tafel slopes of N-doped Co/NF and Co(OH)$_x$/NF precursors without NiFe LDH were 60.0 and 69.5 mV·dec^{-1}, respectively (Fig. S11(c) in the ESM). The Tafel slopes were consistent with the OER activity sequence from the overpotentials, confirming the synergistic effect between the NiFe LDH and N-doped Co to the OER activity. Charge transfer ability was also assessed using EIS. The equivalent circuit diagram of the sample above was fitted based on its Nyquist curve (inset of Fig. 3(d)). This diagram consists of a solution resistance (R_s), a charge-transfer resistance (R_{ct}), and a constant-phase-angle element (CPE). The R_{ct} of NiFe LDH/N-doped Co/NF, NiFe LDH/Co(OH)$_x$/NF, and NiFe LDH/NF at an overpotential of 0.6 V (vs. Hg/HgO) was 0.408, 0.546, and 0.554 Ω, respectively, suggesting that the N-doped Co NWs increased the electron transfer rate for OER effectively. Therefore, the EIS fitting results demonstrated that the Co-based interlayer enhanced the OER activity, confirming the superior OER activity of the NiFe LDH/N-doped Co/NF.

ECSA plays a key role in electrocatalytic performance and the ECSA-normalized specific activity is a valuable metric for evaluating the intrinsic activity of catalytic sites. The C_{dl} was used to estimate the ECSAs of the tested catalysts. Figures S12 and S13 in the ESM present the CV curves measured at various scan rates in the non-Faraday potential region. As shown in Fig. 3(e), the C_{dl} of NiFe-LDH/N-doped Co/NF was 7.4 mF·cm^{-2}, which was higher than those of the NiFe LDH/Co(OH)$_x$/NF (1.3 mF·cm^{-2}) and the NiFe LDH/NF (3.6 mF·cm^{-2}), suggesting that the ECSA significantly increased after the nitridation treatment of the interlayers. The sequence of the C_{dl} values matched the OER activity sequence for the three tested samples, suggesting that the ECSA was positively correlated to the OER activity. Table S2 in the ESM shows the ECSA-normalized OER specific activity at the overpotential of 270 mV for the catalysts. The close specific activity values suggested that the NiFe LDH was the primary active center for OER and the intrinsic activity was not significantly affected by the substrates. Hence, the results demonstrated that ECSA was the dominant factor that affected the overall OER activity for the NiFe LDH-loaded catalysts and the superior activity for the NiFe LDH/N-doped Co/NF was primarily attributed to the high ECSA of the hierarchical structure.

Furthermore, the possible OER active sites of the NiFe LDH/N-doped Co/NF were validated by Raman spectroscopy (Fig. S14 in the ESM). The peaks at 467 and 677 cm^{-1} in the spectra of NiFe LDH/N-doped Co/NF corresponded to the stretching vibrations of M–O, where M represented the metal cations, while the peak at 580 cm^{-1} was attributed to the M–OH vibrations [51]. The two peaks at 215 and 276 cm^{-1} were attributed to the M–O vibrations in LDH [47]. Raman spectroscopy analysis shows that the N-doped Co NW interlayer is well bonded to the surface NiFe LDH.

The NiFe LDH/N-doped Co/NF also exhibited superior OER activity at high current densities, which was important for the industrial water electrolysis, suggesting the facilitated mass transfer, i.e., the accelerated generated oxygen bubble detachment. We performed the contact angle tests on the electrodes. Figure S15 in the ESM shows that the N-doped Co NWs increased the hydrophilicity of the NF substrate, which facilitated bubble detachment and increased the overall efficiency. This superhydrophilic property remained after loading the NiFe LDH catalysts. Thus, the N-doped Co NW interlayer endowed the electrode with hydrophilicity and increased the OER activity, especially at high current densities.

3.3 OER durability

Stability is another crucial criterion for electrocatalysts. As shown in Fig. 3(f), the η_{100} of the NiFe LDH/N-doped Co/NF only increased by 7 mV after 100 h of operation at 100 mA·cm^{-2}. To exclude the possible influence of the accumulated bubbles, a subsequent LSV test (Fig. S16 in the ESM) revealed that the η_{100} increased by only 3 mV, verifying the high stability for the NiFe LDH/N-doped Co/NF. Without the N-doped Co NW interlayer, the NiFe LDH/NF experienced a decay of 20 mV over 100 h (Fig. 3(f)), which was unstable as compared with the NiFe LDH/N-doped Co/NF.

The electrodes after the prolonged stability tests were characterized to demonstrate the origin of the superior stability for the NiFe LDH/N-doped Co/NF. Figures 4(a) and 4(b) show the SEM images of NiFe LDH/N-doped Co/NF after the stability test, demonstrating that the NWs arrays were well-preserved and the NiFe LDH still firmly bonded on the NW arrays without significant destruction. However, the SEM images of the NiFe LDH/NF show that the surface flake morphology of NiFe LDH was almost destroyed, indicating that the interlayer protected the NiFe LDH from degradation effectively (Figs. 4(c) and 4(d)). The structural characterization results demonstrated that the N-doped Co NWs enhanced the structural stability of the NiFe LDH via the strong chemical bond interaction, and the hierarchical array structure would also create fast mass transfer pathways, preventing the mechanical exfoliation of the CLs. XPS results of the samples after the stability tests (Figs. 4(e)–4(h)) revealed that the binding energies of Ni and Fe in NiFe LDH/N-doped Co/NF with N-doped Co NWs negatively shifted as compared to those in NiFe LDH/NF without an interlayer. It suggested that the N-doped Co NW served as an electronic regulator, preventing the over-oxidation of Ni and Fe during OER and thus enhancing stability. The NiFe LDH/N-doped Co/NF was shifted to higher binding energies for both Ni and Fe after the test compared to before the stability test, suggesting that the attenuation was mainly due to the oxidation of the Ni and

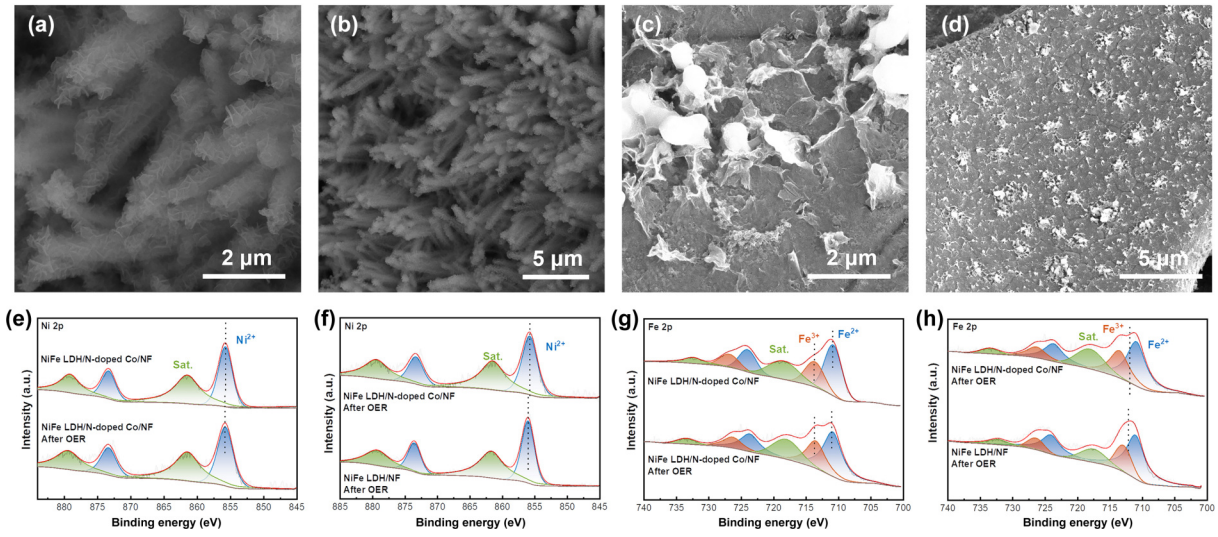

Figure 4 (a) and (b) The SEM images of NiFe LDH/N-doped Co/NF after 100 h stability test. (c) and (d) The SEM images of NiFe LDH/NF after a 100 h stability test. (e) and (f) High-resolution XPS spectra of Ni 2p before and after the stability tests of NiFe LDH/N-doped Co/NF and NiFe LDH/NF. (g) and (h) High-resolution XPS spectra of Fe 2p before and after the stability tests of NiFe LDH/N-doped Co/NF and NiFe LDH/NF.

Fe elements. The Raman spectra of the samples after the stability tests (Fig. S17 in the ESM) show the disappearance of peaks at 216 and 278 cm^{-1}. This was likely due to the conversion of M–O to M–OH during the OER process, which occurred at high potentials [47].

The electrolyte of the stability test was analyzed using ICP-MS to detect dissolved metal ions during the tests (Fig. S18 in the ESM). We found that the dissolution of Fe dominated the NiFe LDH degeneration, and the Fe dissolution in NiFe LDH/N-doped Co/NF was much lower than that in NiFe LDH/NF, suggesting that the N-doped Co NWs effectively inhibited the dissolution of iron and thereby enhanced the stability. Anchoring abundant sites to stabilize the NiFe LDH on the N-doped Co NWs was one of the possible reasons for the low Fe dissolution. Since frustrated mass transfer would result in the decrease of local pH for OER, the facilitated mass transfer by the hierarchical structure might retain the alkaline local environment and thus prevent the catalysts from dissolving. Additionally, the improved electrical conductivity also decreased the overpotential at constant current densities and hindered the anodic corrosion. Therefore, these *ex-situ* characterization results manifested that the interlayer enhanced the OER stability by donating electrons and reinforcing the catalyst–support interaction.

3.4 AEMWE Performance

To demonstrate the application feasibility in AEMWE devices, we set up the water electrolyzer using the NiFe LDH/N-doped Co/NF as the anode, as illustrated in Fig. 5(a). As shown in Fig. S19 in the ESM, we fed 1 M KOH to the cathode and anode runner plates and discharged the KOH solution along with H_2 and O_2 from the other side. The AEMWE device consisted of a metal bipolar plate, a 4 cm^2 stainless steel runner plate, a CCS catalyst, a PTFE gasket, and an anion-exchange membrane, in order from left to right. As shown in Fig. 5(b), the control devices using RuO_2/NF and NiFe foam anodes reach 2.08 and 2.51 $A{\cdot}cm^{-2}$ at 2.0 V, respectively. The device using NiFe LDH/N-doped Co/NF achieved 1 $A{\cdot}cm^{-2}$ at 1.63 V and reached 4.84 $A{\cdot}cm^{-2}$ at 2.0 V, surpassing the control devices at both low and high current densities. Besides the OER activity, mass transfer and ohmic resistance significantly affected the AEMWE performance at the high current densities. The hierarchical structure endowed the NiFe LDH/N-doped Co/NF with the superhydrophilic property, facilitating the mass transfer. The ohmic impedance of the device, including the bipolar plate, runner plate, and CCS with an anion exchange membrane, was measured by EIS. As shown in Fig. 5(c), the ohmic impedance of the device using NiFe LDH/N-doped Co/NF was 76 $m\Omega{\cdot}cm^2$, while the ohmic impedances of the devices using NiFe foam and RuO_2/NF were 91 and 107 $m\Omega{\cdot}cm^2$, respectively. The lowest ohmic impedance of the device using NiFe LDH/N-doped Co/NF manifested the improved conductivity by the N-doped Co NWs, and the device also showed the lowest charge transfer resistance that matched the aforementioned results from the three-electrode system. Therefore, the NiFe LDH/N-doped Co/NF anode exhibited superior AEMWE device performance by simultaneously improving the electrocatalytic kinetics, mass transfer, and electrical conductivity.

Additionally, we tested the AEMWE activity under pure water feeding conditions (Fig. S20 in the ESM). It achieved 1.06 $A{\cdot}cm^{-2}$ at the voltage of 2.0 V, which was comparable with the reported data (Table S3 in the ESM) [52–58], but much lower than that using KOH feeding. The frustrated performance probably resulted from the increased ohmic impedance (ca. 208 $m\Omega{\cdot}cm^2$) with pure water feeding. Hence, the device performance evaluations demonstrated the feasibility of the NiFe LDH/N-doped Co/NF anode in AEMWEs and the superior energy conversion efficiency. We also conducted the stability tests in the AEMWE device, as shown in Fig. 5(d). The device using RuO_2/NF deactivated quickly at the initial 10 h, and the applied voltage increased from 1.86 to 2.03 V at the current density of 1 $A{\cdot}cm^{-2}$, suggesting the poor stability. The device using NiFe LDH/N-doped Co/NF demonstrated good stability with a constant output of 1 $A{\cdot}cm^{-2}$ during over 90 h of continuous operation, showing a voltage increase of 58 mV with a degradation rate of 0.7 $mV{\cdot}h^{-1}$ after the electrolyte refreshment. The stability test in AEMWE devices also verified the feasibility of the top-down construction method of the hierarchical structure for the design of long-life non-precious metal anodes.

4 Conclusions

In summary, this work introduced a top-down construction

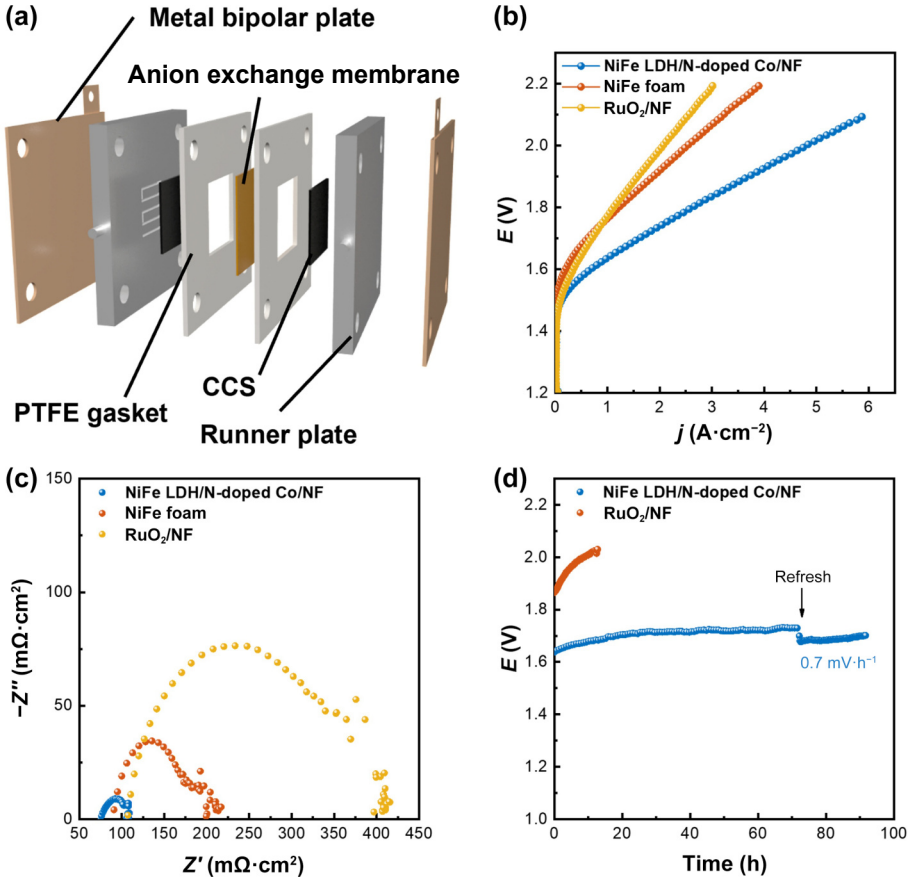

Figure 5 (a) Schematic illustration of AEMWE device. (b) Polarization curves of alkaline electrolyzers of NiFe LDH/N-doped Co/NF, NiFe foam, and RuO_2/NF MEAs at 60 °C in 1 M KOH solution. (c) Nyquist plots of NiFe LDH/N-doped Co/NF, NiFe foam, and RuO_2/NF MEAs. (d) Chronopotentiometric curves of alkaline electrolyzers of NiFe LDH/N-doped Co/NF MEA at a current density of 1 A·cm^{-2}.

strategy for enhancing electrode performance, culminating in the development of a hierarchical NiFe LDH/N-doped Co/NF OER electrocatalyst with exceptional activity and stability for AEMWEs. The NiFe LDH/N-doped Co/NF electrode demonstrated high electrochemical performance, achieving a current density of 100 mA·cm^{-2} at a low overpotential of 262 mV. It also exhibited excellent operational stability, with only a 7 mV increase in overpotential after 100 h of operation at 100 mA·cm^{-2}. When integrated into an AEMWE device, the electrode required merely 1.63 V to sustain a current density of 1 A·cm^{-2} and maintained stable performance over 90 h, underscoring its practical applicability. Comprehensive characterization provided valuable insights into the mechanisms underpinning the enhanced performance of the NiFe LDH/N-doped Co/NF electrode. The introduction of the N-doped Co nanowire interlayer significantly enhanced the ECSA, thereby boosting OER activity. The hierarchical array structure effectively facilitated the mass transfer of oxygen bubbles and electrolytes, while the N-doped Co interlayer improved the conductivity between the nickel foam PTL and the NiFe LDH catalyst CL. Additionally, the interlayer strengthened the stability of the catalyst layer by fostering robust catalyst–support interactions, thereby mitigating Fe leaching and mechanical exfoliation during extended operations. This work presents a synergistic strategy for the design of cost-effective and durable anodes, advancing the practical implementation of AEMWEs and contributing to the development of sustainable hydrogen production technologies.

Electronic Supplementary Material: Supplementary material (SEM, TEM, EDS mapping, XRD, XPS, electrochemical measurements, contact angle measurements, digital picture of AEMWE, performance comparison, etc.) is available in the online version of this article at https://doi.org/10.26599/NR.2025.94907190.

Data availability

All data needed to support the conclusions in the paper are presented in the manuscript and the Electronic Supplementary Material. Additional data related to this paper may be requested from the corresponding author upon request.

Acknowledgements

The authors acknowledge the financial support by the National Key Research and Development Program of China (No. 2022YFA1504000), the National Natural Science Foundation of China (Nos. 22101016 and 22279004), and China National Petroleum Corporation Basic Forward-looking Science and Technology Project (No. 2023ZZ1202).

Declaration of competing interest

All the contributing authors report no conflict of interests in this work.

Author contribution statement

J. S. W.: Data curation, project administration, validation, writing manuscript, experimental design. Y. S. W.: Data curation, validation, experimental design. X. X. G.: Data curation, validation, experimental design. M. T. C.: Data curation, validation, experimental design. J. J. F.: Validation, experimental design, funding acquisition. X. J. L.: Validation, experimental design, funding acquisition. W. Z.: Project administration, validation, writing manuscript, experimental design, funding acquisition. Z. B. Z.: Project administration, validation, writing manuscript, experimental design, funding acquisition. All the authors have approved the final manuscript.

Use of AI statement

None.

References

[1] Sun, H. C.; Zhang, W.; Li, J. G.; Li, Z. S.; Ao, X.; Xue, K. H.; Ostrikov, K. K.; Tang, J.; Wang, C. D. Rh-engineered ultrathin NiFe-LDH nanosheets enable highly-efficient overall water splitting and urea electrolysis. *Appl. Catal. B* **2021**, *284*, 119740.

[2] Zhang, H.; Wang, J.; Qin, F. Q.; Liu, H. L.; Wang, C. Erratum to: V-doped Ni_3N/Ni heterostructure with engineered interfaces as a bifunctional hydrogen electrocatalyst in alkaline solution: Simultaneously improving water dissociation and hydrogen adsorption. *Nano Res.* **2022**, *15*, 7758.

[3] Cheng, J. L.; Wang, D. S. 2D materials modulating layered double hydroxides for electrocatalytic water splitting. *Chin. J. Catal.* **2022**, *43*, 1380–1398.

[4] Gao, Y.; Yang, C. D.; Sun, F. L.; He, D. P.; Wang, X. Q.; Chen, J.; Zheng, X. B.; Liu, R. C.; Pan, H.; Wang, D. S. Ligand-tuning metallic sites in molecular complexes for efficient water oxidation. *Angew. Chem., Int. Ed.* **2024**, *24*, e202415755.

[5] Tang, H. T.; Zhou, H. Y.; Pan, Y. M.; Zhang, J. L.; Cui, F. H.; Li, W. H.; Wang, D. S. Single-atom manganese-catalyzed oxygen evolution drives the electrochemical oxidation of Silane to Silanol. *Angew. Chem., Int. Ed.* **2024**, *63*, e202315032.

[6] Hu, Y. M.; Chao, T. T.; Li, Y. P.; Liu, P. G.; Zhao, T. H.; Yu, G.; Chen, C.; Liang, X.; Jin, H. L.; Niu, S. W. et al. Cooperative Ni(Co)-Ru-P sites activate dehydrogenation for hydrazine oxidation assisting self-powered H_2 production. *Angew. Chem., Int. Ed.* **2023**, *62*, e202308800.

[7] Zhong, B.; Kuang, P. Y.; Wang, L. X.; Yu, J. G. Hierarchical porous nickel supported $NiFeO_xH_y$ nanosheets for efficient and robust oxygen evolution electrocatalyst under industrial condition. *Appl. Catal. B* **2021**, *299*, 120668.

[8] Lin, Y.; Cui, X. J.; Zhao, Y. L.; Liu, Z. C.; Zhang, G. X.; Pan, Y. Heterojunction interface editing in Co/NiCoP nanospheres by oxygen atoms decoration for synergistic accelerating hydrogen and oxygen evolution electrocatalysis. *Nano Res.* **2023**, *16*, 8765–8772.

[9] Zhou, C. A.; Ma, K.; Zhuang, Z. C.; Ran, M. L.; Shu, G. Q.; Wang, C.; Song, L.; Zheng, L. R.; Yue, H. R.; Wang, D. S. Tuning the local environment of Pt species at CNT@MO_{2-x} (M = Sn and Ce) heterointerfaces for boosted alkaline hydrogen evolution. *J. Am. Chem. Soc.* **2024**, *146*, 21453–21465.

[10] Zheng, X. B.; Yang, J. R.; Li, P.; Wang, Q. S.; Wu, J. B.; Zhang, E. H.; Chen, S. H.; Zhuang, Z. C.; Lai, W. H.; Dou, S. X. et al. Ir-Sn pair-site triggers key oxygen radical intermediate for efficient acidic water oxidation. *Sci. Adv.* **2023**, *9*, eadi8025.

[11] Zheng, X. B.; Yang, J. R.; Xu, X.; Dou, S. X.; Sun, W. P.; Wang, D. S.; Wang, G. X. Deciphering cationic and anionic overoxidation: Key insights into the intrinsic structural degradation of catalysts. *Adv. Energy Mater.* **2024**, *14*, 2401227.

[12] Feng, L.; Xue, H. G. Advances in transition-metal phosphide applications in electrochemical energy storage and catalysis. *ChemElectroChem* **2017**, *4*, 20–34.

[13] Luo, H. Z.; Zeng, Z. T.; Zeng, G. M.; Zhang, C.; Xiao, R.; Huang, D. L.; Lai, C.; Cheng, M.; Wang, W. J.; Xiong, W. P. et al. Recent progress on metal-organic frameworks based- and derived-photocatalysts for water splitting. *Chem. Eng. J.* **2020**, *383*, 123196.

[14] Chen, P. Z.; Hu, X. L. High-efficiency anion exchange membrane water electrolysis employing non-noble metal catalysts. *Adv. Energy Mater.* **2020**, *10*, 2002285.

[15] Wan, L.; Liu, J.; Lin, D. C.; Xu, Z.; Zhen, Y. H.; Pang, M. B.; Xu, Q.; Wang, B. G. 3D-ordered catalytic nanoarrays interlocked on anion exchange membranes for water electrolysis. *Energy Environ. Sci.* **2024**, *17*, 3396–3408.

[16] Li, H. J. W.; Lin, Y.; Duan, J. Y.; Wen, Q. L.; Liu, Y. W.; Zhai, T. Y. Stability of electrocatalytic OER: From principle to application. *Chem. Soc. Rev.* **2024**, *53*, 10709–10740.

[17] Guo, Y. J.; Liu, Z. Y.; Zhou, D. Y.; Zhang, M. Y.; Zhang, Y.; Li, R. Z.; Liu, S. L.; Wang, D. S.; Dai, Z. H. Competition and synergistic effects of Ru-based single-atom and cluster catalysts in electrocatalytic reactions. *Sci. China Mater.* **2024**, *67*, 1706–1720.

[18] Mu, X. Q.; Liu, S. L.; Zhang, M. Y.; Zhuang, Z. C.; Chen, D.; Liao, Y. R.; Zhao, H. Y.; Mu, S. C.; Wang, D. S.; Dai, Z. H. Symmetry-broken Ru nanoparticles with parasitic Ru-Co dual-single atoms overcome the volmer step of alkaline hydrogen oxidation. *Angew. Chem., Int. Ed.* **2024**, *63*, e202319618.

[19] Mu, X. Q.; Yu, M.; Liu, X. Y.; Liao, Y. R.; Chen, F. J.; Pan, H. Z.; Chen, Z. Y.; Liu, S. L.; Wang, D. S.; Mu, S. C. High-entropy ultrathin amorphous metal-organic framework-stabilized Ru(Mo) dual-atom sites for water oxidation. *ACS Energy Lett.* **2024**, *9*, 5763–5770.

[20] Chen, R.; Hung, S. F.; Zhou, D. J.; Gao, J. J.; Yang, C. J.; Tao, H. B.; Yang, H. B.; Zhang, L. P.; Zhang, L. L.; Xiong, Q. H. et al. Layered structure causes bulk NiFe layered double hydroxide unstable in alkaline oxygen evolution reaction. *Adv. Mater.* **2019**, *31*, 1903909.

[21] Gong, L. Q.; Yang, H.; Douka, A. I.; Yan, Y.; Xia, B. Y. Recent progress on NiFe-based electrocatalysts for alkaline oxygen evolution. *Adv. Sustain. Syst.* **2021**, *5*, 2000136.

[22] Wu, Z. P.; Lu, X. F.; Zang, S. Q.; Lou, X. W. Non-noble-metal-based electrocatalysts toward the oxygen evolution reaction. *Adv. Funct. Mater.* **2020**, *30*, 1910274.

[23] Chen, Y. F.; Li, J. H.; Liu, T. T.; You, S. H.; Liu, P.; Li, F. J.; Gao, M. Q.; Chen, S. G.; Zhang, F. F. Constructing robust NiFe LDHs–NiFe alloy gradient hybrid bifunctional catalyst for overall water splitting: One-step electrodeposition and surface reconstruction. *Rare Met.* **2023**, *42*, 2272–2283.

[24] Shen, K. Y.; Tang, Y.; Zhou, Q. H.; Zhang, Y.; Ge, W.; Shai, X. X.; Deng, S. P.; Yang, P. Z.; Deng, S. K.; Wang, J. S. Metal-organic framework-derived S-NiFe PBA coupled with NiFe layered double hydroxides as Mott-Schottky electrocatalysts for efficient alkaline oxygen evolution reaction. *Chem. Eng. J.* **2023**, *471*, 144827.

[25] Li, Y. X.; Liu, J. L.; Li, S. Q.; Peng, S. Q. Codecoration of phosphate and iron for improving oxygen evolution reaction of layered $Ni(OH)_2$/NiOOH. *ACS Catal.* **2024**, *14*, 4807–4819.

[26] Liu, S. Q.; Qi, W. L.; Liu, J.; Meng, X. L.; Adimi, S.; Attfield, J. P.; Yang, M. H. Modulating electronic structure to improve the solar to hydrogen efficiency of cobalt nitride with lattice doping. *ACS Catal.* **2023**, *13*, 2214–2222.

[27] Song, Y. F.; Zhang, Z. Y.; Tian, H.; Bian, L.; Bai, Y.; Wang, Z. L. Corrosion engineering towards NiFe-layered double hydroxide macroporous arrays with enhanced activity and stability for oxygen evolution reaction. *Chem.—Eur. J.* **2023**, *29*, e202301124.

[28] Zhang, Y.; Feng, B.; Yan, M. L.; Shen, Z.; Chen, Y. Q.; Tian, J. Y.; Xu, F. F.; Chen, G. H.; Wang, X. Z.; Yang, L. J. et al. Self-supported NiFe-LDH nanosheets on NiMo-based nanorods as high-performance bifunctional electrocatalysts for overall water splitting at industrial-level current densities. *Nano Res.* **2024**, *17*, 3769–3776.

[29] Wang, Y. H.; Li, S. Q.; Hou, X.; Cui, T. T.; Zhuang, Z. C.; Zhao, Y. H.; Wang, H. Z.; Wei, W.; Xu, M.; Fu, Q. et al. Low-spin Fe^{3+} evoked by multiple defects with optimal intermediate adsorption attaining unparalleled performance in water oxidation. *Adv. Mater.* **2024**, *14*, 2412598.

[30] Zhang, J. F.; Liu, J. Y.; Xi, L. F.; Yu, Y. F.; Chen, N.; Sun, S. H.; Wang, W. C.; Lange, K. M.; Zhang, B. Single-atom Au/NiFe layered double hydroxide electrocatalyst: Probing the origin of activity for oxygen evolution reaction. *J. Am. Chem. Soc.* **2018**, *140*, 3876–3879.
[31] Zheng, Z. C.; Wu, D.; Chen, G.; Zhang, N.; Wan, H.; Liu, X. H.; Ma, R. Z. Microcrystallization and lattice contraction of NiFe LDHs for enhancing water electrocatalytic oxidation. *Carbon Energy* **2022**, *4*, 901–913.
[32] Xing, M. H.; Qiao, Z. L.; Zhu, S. K.; Xu, G. Q.; Yun, J.; Cao, D. P. Zipper-like interlocked heterostructure of NiFe layered double hydroxide-WN for super-stable oxygen evolution over 4500 h. *Adv. Funct. Mater.* **2024**, *34*, 2409559.
[33] Wang, M.; Zhang, W. J.; Zhang, F. F.; Zhang, Z. H.; Tang, B.; Li, J. P.; Wang, X. G. Theoretical expectation and experimental implementation of *in situ* Al-doped CoS_2 nanowires on dealloying-derived nanoporous intermetallic substrate as an efficient electrocatalyst for boosting hydrogen production. *ACS Catal.* **2019**, *9*, 1489–1502.
[34] Bhosale, A. C.; Ghosh, P. C.; Assaud, L. Preparation methods of membrane electrode assemblies for proton exchange membrane fuel cells and unitized regenerative fuel cells: A review. *Renew. Sustain. Energy Rev.* **2020**, *133*, 110286.
[35] Wang, B.; Tang, C.; Wang, H. F.; Chen, X.; Cao, R.; Zhang, Q. A Nanosized CoNi hydroxide@hydroxysulfide core–shell heterostructure for enhanced oxygen evolution. *Adv. Mater.* **2019**, *31*, 1805658.
[36] Yu, L.; Zhou, H. Q.; Sun, J. Y.; Qin, F.; Yu, F.; Bao, J. M.; Yu, Y.; Chen, S.; Ren, Z. F. Cu nanowires shelled with NiFe layered double hydroxide nanosheets as bifunctional electrocatalysts for overall water splitting. *Energy Environ. Sci.* **2017**, *10*, 1820–1827.
[37] Jeon, S. S.; Lim, J.; Kang, P. W.; Lee, J. W.; Kang, G.; Lee, H. Design principles of NiFe-layered double hydroxide anode catalysts for anion exchange membrane water electrolyzers. *ACS Appl. Mater. Interfaces* **2021**, *13*, 37179–37186.
[38] Long, X.; Wang, Z. L.; Xiao, S.; An, Y. M.; Yang, S. H. Transition metal based layered double hydroxides tailored for energy conversion and storage. *Mater. Today* **2016**, *19*, 213–226.
[39] Todoroki, N.; Kudo, R.; Hayashi, K.; Yokoi, M.; Naraki, N.; Wadayama, T. Improving the oxygen evolution activity and stability of Nb-doped TiO_2-supported RuO_2 by a SnO_2 interlayer: A model catalyst study on single-crystal oxide heterostructures. *ACS Catal.* **2023**, *13*, 11433–11440.
[40] Liang, C. W.; Zou, P. C.; Nairan, A.; Zhang, Y. Q.; Liu, J. X.; Liu, K. W.; Hu, S. Y.; Kang, F. Y.; Fan, H. J.; Yang, C. Exceptional performance of hierarchical Ni-Fe oxyhydroxide@NiFe alloy nanowire array electrocatalysts for large current density water splitting. *Energy Environ. Sci.* **2020**, *13*, 86–95.
[41] Lv, J. J.; Wang, L. M.; Li, R. S.; Zhang, K. Y.; Zhao, D. F.; Li, Y. Q.; Li, X. J.; Huang, X. B.; Wang, G. Constructing a hetero-interface composed of oxygen vacancy-enriched Co_3O_4 and crystalline-amorphous NiFe-LDH for oxygen evolution reaction. *ACS Catal.* **2021**, *11*, 14338–14351.
[42] Wang, M. H.; Lou, Z. X.; Wu, X. F.; Liu, Y. W.; Zhao, J. Y.; Sun, K. Z.; Li, W. X.; Chen, J. C.; Yuan, H. Y.; Zhu, M. H. et al. G. *Operando* high-valence Cr-modified NiFe hydroxides for water oxidation. *Small* **2022**, *18*, 2200303.
[43] He, L. X.; Wang, N.; Sun, B. L.; Zhong, L.; Yao, M. Q.; Hu, W. C.; Komarneni, S. High-entropy FeCoNiMn (oxy)hydroxide as high-performance electrocatalyst for OER and boosting clean carrier production under quasi-industrial condition. *J. Clean. Prod.* **2022**, *356*, 131680.
[44] Chen, M. P.; Liu, D.; Feng, J. X.; Zhou, P. F.; Qiao, L. L.; Feng, W. L.; Chen, Y. Y.; Ng, K. W.; Wang, S. P.; Ip, W. F. et al. *In-situ* generation of Ni-CoOOH through deep reconstruction for durable alkaline water electrolysis. *Chem. Eng. J.* **2022**, *443*, 136432.
[45] Du, Y.; Zhou, Y.; Zhao, Q.; Zhou, Y. J.; Chen, Y. K.; Jiang, T. S. Nano-assembly hierarchical Fe-Ni-Se/$Cu(OH)_2$ with induced interface engineering as highly efficient electrocatalyst for oxygen evolution reaction. *Electrochim. Acta* **2022**, *413*, 140186.
[46] Zhang, H. L.; Li, Y. Y.; Zhao, J. Y.; Zhang, Y.; Zhang, H. T.; Song, R. Hierarchical Cu_2O/NiFeCo layered double hydroxide nanoarrays on copper foam obtained by a self-sacrificial templated route for a highly efficient oxygen evolution reaction. *J. Colloid Interface Sci.* **2023**, *630*, 695–703.
[47] Chen, B. J.; Humayun, M.; Li, Y. D.; Zhang, H. M.; Sun, H. C.; Wu, Y.; Wang, C. D. Constructing hierarchical fluffy CoO-Co_4N@NiFe-LDH nanorod arrays for highly effective overall water splitting and urea electrolysis. *ACS Sustain. Chem. Eng.* **2021**, *9*, 14180–14192.
[48] Jiang, J.; Sun, F. F.; Zhou, S.; Hu, W.; Zhang, H.; Dong, J. C.; Jiang, Z.; Zhao, J. J.; Li, J. F.; Yan, W. S. et al. Atomic-level insight into super-efficient electrocatalytic oxygen evolution on iron and vanadium co-doped nickel (oxy)hydroxide. *Nat. Commun.* **2018**, *9*, 2885.
[49] Li, J. H.; Wang, L. L.; He, H. J.; Chen, Y. Q.; Gao, Z. R.; Ma, N.; Wang, B.; Zheng, L. L.; Li, R. L.; Wei, Y. J. et al. Interface construction of NiCo LDH/NiCoS based on the 2D ultrathin nanosheet towards oxygen evolution reaction. *Nano Res.* **2022**, *15*, 4986–4995.
[50] Zeng, L. Y.; Sun, K. A.; Wang, X. B.; Liu, Y. Q.; Pan, Y.; Liu, Z.; Cao, D. W.; Song, Y.; Liu, S. H.; Liu, C. G. Three-dimensional-networked Ni_2P/Ni_3S_2 heteronanoflake arrays for highly enhanced electrochemical overall-water-splitting activity. *Nano Energy* **2018**, *51*, 26–36.
[51] Zaffora, A.; Megna, B.; Seminara, B.; Di Franco, F.; Santamaria, M. Ni,Fe,Co-LDH coated porous transport layers for zero-gap alkaline water electrolyzers. *Nanomaterials* **2024**, *14*, 407.
[52] Zheng, Y. W.; Serban, A.; Zhang, H. Y.; Chen, N. J.; Song, F.; Hu, X. L. Anion exchange ionomers enable sustained pure-water electrolysis using platinum-group-metal-free electrocatalysts. *ACS Energy Lett.* **2023**, *8*, 5018–5024.
[53] Zhang, L. Y.; Xu, Q. C.; Wen, S. T.; Zhang, H. X.; Chen, L.; Jiang, H.; Li, C. Z. Recycling spent ternary cathodes to oxygen evolution catalysts for pure water anion-exchange membrane electrolysis. *ACS Nano* **2024**, *18*, 22454–22464.
[54] Yang, X. X.; Liang, J. S.; Shi, Q. R.; Zachman, M. J.; Kabir, S.; Liang, J. W.; Zhu, J.; Slenker, B.; Pupucevski, M.; Macauley, N. et al. Regulating the third metal to design and engineer multilayered NiFeM (M: Co, Mn, and Cu) nanofoam anode catalysts for anion-exchange membrane water electrolyzers. *Adv. Energy Mater.* **2024**, *14*, 2400029.
[55] Thangavel, P.; Lee, H.; Kong, T. H.; Kwon, S.; Tayyebi, A.; Lee, J. H.; Choi, S. M.; Kwon, Y. Immobilizing low-cost metal nitrides in electrochemically reconstructed platinum group metal (PGM)-free oxy-(hydroxides) surface for exceptional OER kinetics in anion exchange membrane water electrolysis. *Adv. Energy Mater.* **2023**, *13*, 2203401.
[56] Abed, J.; Ahmadi, S.; Laverdure, L.; Abdellah, A.; O'Brien, C. P.; Cole, K.; Sobrinho, P.; Sinton, D.; Higgins, D.; Mosey, N. J. et al. *In situ* formation of nano Ni-Co oxyhydroxide enables water oxidation electrocatalysts durable at high current densities. *Adv. Mater.* **2021**, *33*, 2103812.
[57] Shi, Y.; Song, L. M.; Liu, Y.; Wang, T. T.; Li, C. X.; Lai, J. P.; Wang, L. Dual cocatalytic sites synergize NiFe layered double hydroxide to boost oxygen evolution reaction in anion exchange membrane water electrolyzer. *Adv. Energy Mater.* **2024**, *14*, 2402046.
[58] Jiang, W.; Faid, A. Y.; Gomes, B. F.; Galkina, I.; Xia, L.; Lobo, C. M. S.; Desmau, M.; Borowski, P.; Hartmann, H.; Maljusch, A. et al. Composition-dependent morphology, structure, and catalytical performance of nickel-iron layered double hydroxide as highly-efficient and stable anode catalyst in anion exchange membrane water electrolysis. *Adv. Energy Mater.* **2022**, *32*, 2203520.